JOURNAL OF PROPULSION AND POWER
Vol. 24, No. 2, March–April 2008

Real-Gas Effects in Organic Rankine Cycle Turbine Nozzles

P. Colonna* and J. Harinck†
Delft University of Technology, 2628 California Delft, The Netherlands
S. Rebay‡
Università degli Studi di Brescia, 25123 Brescia, Italy
and
A. Guardone§
Politecnico di Milano, 20159 Milano, Italy

DOI: 10.2514/1.29718

Organic Rankine cycle turbogenerators are a viable option as stationary energy converters for external heat sources, in the low power range (from a few kW up to a few MW). The fluid-dynamic design of organic Rankine cycle turbines can benefit from computational fluid dynamics tools which are capable of properly taking into account real-gas effects occurring in the turbine, which typically expands in the nonideal-gas thermodynamic region. In addition, the potential efficiency increase offered by supercritical organic Rankine cycles, which entails even stronger real-gas effects, has not yet been exploited in current practice. In this paper, real-gas effects occurring in subcritical and supercritical organic Rankine cycle nozzles have been investigated. Two-dimensional Euler simulations of an existing axial organic Rankine cycle stator nozzle are carried out using a computational fluid dynamics code, which is linked to an accurate thermodynamic model for the working fluid (octamethyltrisiloxane $C_8H_{24}O_2Si_3$). The cases analyzed include the expansions starting from actual subcritical conditions, that is, the design point and part-load operation, and three expansions starting from supercritical conditions. Results of the simulations of the existing nozzle for current operating conditions can be used to refine its design. Moreover, the simulations of the nozzle expansions starting from supercritical conditions show that a nozzle geometry with a much higher exit-to-throat area ratio is required to obtain an efficient expansion. Other peculiar characteristics of supercritical expansions such as low sound speed and velocity, high density, and mass flow rate, are discussed.

Nomenclature

A	=	cross-sectional area
C	=	specific heat, blade chord, coefficient
c	=	speed of sound
h	=	static enthalpy
M	=	molecular weight
$\dot{m}$	=	mass flow rate
n	=	parameter in Span–Wagner equation of state
P	=	pressure, power
R	=	specific gas constant
$\mathcal{R}$	=	universal gas constant
S	=	curvilinear distance along the blade profile
s	=	entropy
T	=	temperature
u	=	velocity
v	=	specific volume
X	=	nozzle axial coordinate
Z	=	compressibility factor
γ	=	ratio of specific heat capacities
Δ	=	difference
δ	=	reduced density
η	=	efficiency
ρ	=	density
τ	=	inverse of reduced temperature
ψ	=	reduced Helmholtz energy

Subscripts

A	=	turbine inlet total
ax	=	axial
B	=	turbine outlet
cr	=	critical point
D	=	condensor outlet
e	=	electric
G	=	flue gas inlet
gen	=	electric generator
I	=	cooling water inlet
i	=	ideal gas
is	=	isentropic
K	=	cooling water outlet
max	=	cycle maximum
P	=	isobaric
PHE	=	primary heat exchanger
PL	=	pressure loss
p	=	pump
pinch	=	pinch point
r	=	exit-to-throat ratio
re	=	real gas
regen	=	regenerator
t	=	nozzle throat, turbine
v	=	isochoric
x	=	nozzle axial coordinate
0	=	total (or stagnation)
1	=	nozzle inlet
2	=	nozzle exit

Superscripts

L	=	saturated liquid
r	=	real-gas contribution

Received 12 January 2007; revision received 17 September 2007; accepted for publication 20 September 2007.

*Associate Professor, Energy Technology Section, Process and Energy Department, Leeghwaterstraat 44; p.colonna@tudelft.nl.
†Ph.D. Candidate, Energy Technology Section, Process and Energy Department, Leeghwaterstraat 44; j.harinck@tudelft.nl.
‡Associate Professor, Dipartimento di Ingegneria Meccanica, Via Branze, 38; rebay@ing.unibs.it.
§Assistant Professor, Dipartimento di Ingegneria Aerospaziale, Via La Masa 34; guardone@aero.polimi.it.

sat	=	saturation
V	=	saturated vapor
0	=	ideal-gas contribution

I. Introduction

ORGANIC Rankine cycle (ORC) turbogenerators are a viable option as stationary energy converters for external heat sources, in the low power range (from a few kW up to a few MW). The working principle of an ORC turbogenerator is the same as for a conventional steam power plant, except for the working fluid, which is formed by organic molecules. The choice of the fluid allows for the optimal design of the turbine, depending on the temperature of the heat source and the power range [1–3]. Steam turbines in the low power range cannot reach the same level of efficiency of ORC turbines with the same level of technology. The optimal design of a steam turbine for such a low power range requires many stages, small blade dimensions, and very high rotational speeds, which in turn may lead to severe efficiency problems if the flow becomes locally supersonic and shocks may occur in the flowfield. On the contrary, a turbine operated with an organic fluid can reach very high isentropic efficiency with just one or two stages rotating at a much lower speed. In some cases the turbine can be directly coupled to the electrical generator (3000 rpm). Other advantages with respect to steam cycle turbines include the following [4–6]:

1) Fully dry expansion: superheating can be avoided and there is no efficiency loss associated with condensation in the last stage of the turbine.

2) Moderate maximum pressure: requirements on materials are far less stringent.

3) Possibly higher pressure in the condenser: depending on the fluid, the condenser can be superatmospheric, therefore avoiding the need for a dearator.

4) In some cases the working fluid can also be used as a lubricant for the turbine.

5) Overall very high reliability: the plants are usually fully automated and can sustain unattended operation.

The main thermodynamic restriction affecting ORC technology is the limit on the maximum cycle temperature, which is bound by the thermal stability of the fluid in combination with the containing material. However, in this power range techno-economic constraints would limit the maximum temperature of steam cycles to a level comparable to the thermal stability of ORC working fluids in stainless steel, that is, between 300 and 400°C.

ORC turbogenerators with an installed power adding up to $\sim$8500 MW_e are employed to convert low grade geothermal heat into electricity and so-called low-temperature ORC technology can be considered mature [7,8]. Recent projections indicate that the potential for the application of such a technology is globally

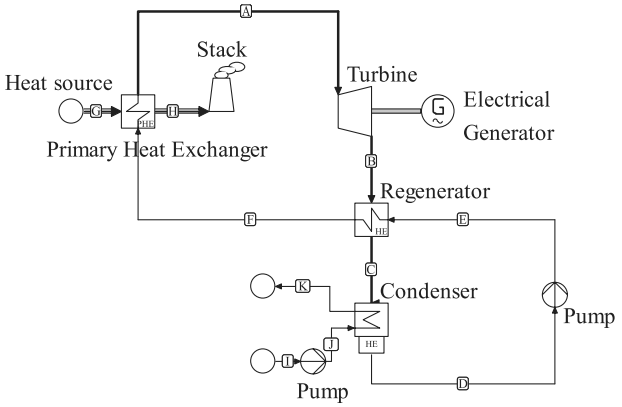

Fig. 1 Process flow diagram of an organic Rankine cycle turbogenerator.

$\sim$60,000 MW_e [9]. The working fluids for these applications are usually hydrocarbons of the alkanes class and refrigerants like R134a or R245fa. Heat source temperatures range from less than 100 up to 150°C (pressurized geothermal water).

More recently, ORC turbogenerators are rapidly spreading as energy converters for biomass fuels, most often in combined-heat-and-power (CHP) applications [10,11]. Transportation costs for biomass dictate a small design power output, if the aim is the conversion of its calorific content into electricity. Presently, ORC technology is possibly the best option in the small power range. The working fluids currently adopted for high-temperature ORC plants are the light members of the siloxanes class and toluene. The maximum cycle temperature ranges from approximately 260°C up to more than 300°C.

It can be noted that the mentioned applications of ORC technology can all be classified as sustainable, and this technology is also very promising for the conversion into electricity of other fully sustainable energy sources, such as solar radiation [12] and waste heat recovery from industrial processes, other engines and, in the future, high-temperature fuel cells [13,14]. ORCs coupled with solar concentrators were considered in the past as a viable option to power the international space station [15–20], and also, coupled with a nuclear isotope heat source [21,22], for deep-space missions.

The process flow diagram of an ORC is depicted in Fig. 1. The corresponding thermodynamic cycle is represented in the T–s plane in Fig. 2a: in this exemplary case of a high-temperature ORC, the working fluid is octamethyltrisiloxane (MDM, $C_8H_{24}O_2Si_3$), which also corresponds to the fluid chosen for the analyses presented in this paper.

The motivation for this study stems from two considerations. First, the fluid-dynamic design of ORC turbines has possibly reached a far

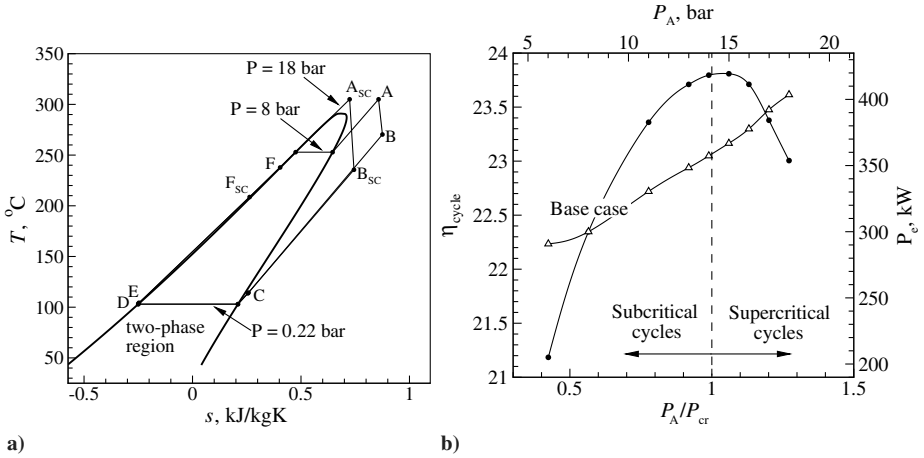

Fig. 2 a) Superheated and supercritical (SC) ORC in the temperature-entropy diagram of siloxane MDM. b) Cycle efficiency (●) and electric power output (△) as functions of turbine inlet pressure. All other design parameters except the maximum cycle pressure and power output are kept fixed and their values are listed in Table 1.

lower level of sophistication, if compared to gas or steam turbines. One of the reasons is the lack of computational fluid dynamics (CFD) tools capable of properly taking into account real-gas effects in the computation of thermodynamic properties, a necessary feature for the accurate design of ORC blade passages. Second, a considerable improvement in efficiency could be reached by resorting to supercritical cycle configurations [4,5,13,16]. This option is still widely unexplored and all existing applications employ either the saturated or the slightly superheated cycle configuration. Reaching supercritical operating conditions in an ORC presents far lower technological challenges, if compared to steam power plants because pressures would be 1 order of magnitude smaller and temperatures would still be considered mild. Among the research needs which must be addressed, the fluid-dynamic design of unconventional supercritical turbines demands for CFD tools capable of simulating flows occurring in a highly nonideal thermodynamic region. This work represents a first step in this direction.

The numerical simulation of compressible flows occurring in a thermodynamic region characterized by strong deviations from the so-called ideal-gas behavior is a research field which is possibly still in its infancy (see, e.g., [23]). A quite comprehensive review can be found, for example, in [24], where the CFD software tool adopted in this study is also described and validated. To the knowledge of the authors the only reference directly related to this work [25] shows the results of fluid-dynamic simulations of the rotor of a centrifugal ORC turbine employing toluene as the working fluid.

This work takes as an exemplary starting point the geometry of an existing ORC nozzle designed for a 300 kW_e CHP axial turbogenerator employing siloxane MDM as working fluid and the combustion of biomass as a primary energy source. A brief overview regarding the thermodynamic efficiency of supercritical ORC cycles is presented in the following section. Here also some technical aspects are shortly addressed. The recently developed thermodynamic model of the working fluid is summarized in Sec. III. Section IV contains a quasi-one-dimensional analysis of supersonic expansions through converging–diverging nozzles, which can be used as the basis for setting appropriate boundary conditions for the design of multidimensional turbine blades. The core of this work is formed by the fluid flow simulations and their analysis shown in Sec. V. Several cases are examined: the base case is the simulation of the flow occurring for design operating parameters. The usefulness of the software tool is demonstrated further by the analysis of the flow for part-load operation. Finally, the flow through the same geometry is simulated for three operating conditions featuring the inflow at supercritical conditions. The analysis of the results can be used as a starting point for the design of such unconventional turbines. The concluding section summarizes the main issues and outlines future lines of investigation.

II. Supercritical Cycle Configurations

To quantify the possible efficiency increase of supercritical ORCs, a brief thermodynamic analysis of the influence of the maximum cycle pressure on the cycle performance is presented. The operating parameters for the base case, given in Table 1, are typical of an existing biomass fueled plant, cogenerating warm water for process purposes. The cycle process is represented in Fig. 2a. It is a superheated cycle in which the amount of superheating has been increased ($T_{\max} = 305°C$) with respect to the current design ($T_{\max} = 270.5°C$), so that the maximum temperature can be kept fixed. This allows for a parametric study of the influence of the maximum pressure solely. Such a maximum temperature is still within the thermal stability limit of the fluid [3,16] and it could be reached if, for instance, the current practice of adopting an intermediate thermal oil loop were abandoned in favor of higher efficiency.

The calculations are carried out with Cycle Tempo [26], an extensively tested software package for the design and analysis of energy conversion systems. The same thermodynamic library [27] that is linked to the CFD code employed in this study is also linked to this steady-state system simulation software. The thermodynamic model for the working fluid MDM contained in the library is described in Sec. III. Typical design values were used as input data for the isentropic efficiencies of the turbine and the pump, and for the pinch points of the heat exchangers. The operating conditions of the cycle and the assumed component efficiencies are listed in Table 1. The given condensation temperature is typical of cogeneration applications. The maximum temperature is limited by the thermal stability of the fluid, taking into account a certain safety margin. Subsequently, the maximum cycle pressure is increased, keeping constant all conditions mentioned in Table 1. In Fig. 2a both the superheated and supercritical (SC) thermodynamic cycles (with a turbine inlet total pressure of $P_A = 18$ bar) are depicted in a T–s diagram.

Table 1 Possible ORC design-point operating conditions for cogeneration of electricity and warm water. The working fluid is siloxane MDM

Working fluid		MDM
Power output	P_e, kW	300
Turbine inlet total pressure	P_A, bar	8
Turbine inlet total temperature	T_A, °C	305
Pressure ratio	P_A/P_B	36
Condensation pressure	P_D, bar	0.22
Condensation temperature	T_D, °C	103
Regenerator pressure loss	ΔP_{regen}, bar	0.1
Flue gas inlet temperature	T_G, °C	350
Flue gas mass flow rate	$\dot{m}_G$, kg/s	12.5
Primary heat exchanger pinch point	$\Delta T_{\text{pinch,PHE}}$, °C	15
Regenerator pinch point	$\Delta T_{\text{pinch,regen}}$, °C	10
Cooling water temperature inlet	T_I, °C	60
Cooling water temperature outlet	T_K, °C	90
Turbine isentropic efficiency	$\eta_{\text{is},t}$	0.87
Pump isentropic efficiency	$\eta_{\text{is},p}$	0.65
Electric generator efficiency	η_{gen}	0.98

The first-law total cycle efficiency, defined as the ratio of the net delivered mechanical power and the heat added to the cycle in the primary heat exchanger, together with the electrical power output, are plotted as a function of the maximum cycle pressure, that is, the turbine inlet total pressure, in Fig. 2b. Figure 2b shows that the cycle efficiency increases with pressure and has a maximum for slightly supercritical conditions. The power output increases steadily with the maximum cycle pressure, the only limiting factor being avoiding condensation throughout the expansion.

As a consequence of the improved heat source utilization, a larger primary heat exchanger is required in case of a supercritical ORC. The regenerated heat decreases only marginally, so that the required regenerator size remains approximately the same. The turbine expansion ratio increases and, as apparent from Fig. 2a, the temperature drop over the turbine also becomes larger, indicating a correspondingly larger enthalpy drop, which may necessitate a multistage turbine and thus higher investment cost. The increase in pressure means a much higher pump power consumption; therefore pump efficiency and investment cost become more important cost-determining factors. Apart from the design of turbines expanding from supercritical inlet conditions, other areas of research demand include supercritical heat exchangers and possibly new control strategies.

III. Thermodynamic Model

The working medium of the ORC in this study, the siloxane MDM (octamethyltrisiloxane), has a high molecular weight of $M = 236.53$ g/mol. Its critical pressure and temperature are $P_{\text{cr}} = 14.2$ bar and $T_{\text{cr}} = 290.9°C$, respectively [28]. A part of the processes in the cycle simulations and flow simulations presented in this study occur at close-to-critical or supercritical conditions and are therefore thermodynamically highly nonideal. For this reason, all thermodynamic property evaluations are based on a state-of-the-art multiparameter functional form for equations of state (MPEoS) developed by Span and Wagner [29]. This MPEoS allows for

Table 2 Performance of the Span–Wagner EoS regarding the prediction of experimental thermodynamic data of MDM. The performance is assessed by means of the average percentage deviation (DEV) of experimental data with respect to computed values; adapted from [32]

Property	Source	P range, bar	T range, K	DEV, %
Saturated liquid density, ρ^L	Lindley and Hershey [33]	——	426–564	0.56
	Hurd [34]	——	273–333	0.12
Saturated vapor density, ρ^V	Lindley and Hershey [33]	——	460–564	0.84
Vapor pressure, P^{sat}	Flaningam [35]	——	346–436	0.46
	Lindley and Hershey [33]	——	322–564	0.66
	Skorokhodov et al. [36]	——	344–418	9.67
P–ρ–T data in the superheated vapor region	Marcos et al. [37]	0.36–3.77	448–573	0.60
P–ρ–T data in the subcooled liquid region	McLure et al. [38]	1.01325	300–412	0.00

accurate computations of all relevant thermodynamic properties over the entire thermodynamic range (even close to the critical point) with the accuracy required for design and analysis of advanced technical applications. The Span–Wagner (SW) EoS has superior accuracy and numerical stability compared with older MPEoSs [29].

Recently, work has been done on the development of 12-parameter SW-type EoSs for selected siloxanes [30,31]. Parameters for a SW-type EoS were also recently optimized for siloxane MDM, the working medium of the ORC in this study [32]. Details about the functional forms and features of the equation of state applied to siloxanes can be found in [30]. A comparison of the predictions of this multiparameter equation of state (MPEoS) with experimental data, given in Table 2, shows very good agreement. Further details are provided in a paper that has been submitted for publication.

For the calculation of all caloric properties, the SW EoS is supplemented by the ideal-gas contribution to the specific heat at constant pressure, which has been approximated here as a polynomial function of the temperature:

$$C_P^0(T) = A + BT + CT^2 + DT^3 \tag{1}$$

The polynomial coefficients for selected siloxanes have been first reported in a work describing the thermodynamic optimization of ORCs [39] and these parameters were recently refined by means of experimental measurements and ab initio molecular simulations [40].

IV. Quasi-One-Dimensional Isentropic Flow Analysis for Subcritical and Supercritical Inlet Pressures

In this section, the effect of an increase in the inlet total pressure on the isentropic expansion process in the ORC turbine is investigated by considering quasi-one-dimensional isentropic flow in a converging–diverging nozzle. As is well known, the isentropic transformation based on the ideal-gas law states that the Mach number is dependent only on the ratio of static exit-to-total inlet pressure and on the ratio of specific heats. However, in the case of an ORC expansion, typically occurring in the dense-gas region, the ideal-gas law is not valid. This is even more so for expansions that occur at close-to-critical and supercritical pressures. For this reason, the analysis is based on the accurate SW EoS [Eq. (1)] that was discussed in the previous section.

The isentropic gas flow through a nozzle of variable cross-sectional area $A = A(x)$ can be computed by means of the mass and energy conservation equations, which, for an arbitrary section x of the duct, can be written as

$$(\rho u A)_x = \text{const} \qquad (h + \tfrac{1}{2}u^2)_x = h_{0x} = \text{const}$$

These equations are here used to show that the exit-to-throat area ratio $A_r = A_2/A_t$ is a function of the pressure ratio $P_r = P_{01}/P_2$, the inlet total pressure P_{01}, and the entropy s. Notice that, as is well known, in the ideal-gas case A_r is instead a function of P_r only, and is given by

$$A_r = P_r^{\frac{1}{\gamma}}\left[\frac{2}{\gamma-1}\left(\frac{\gamma+1}{2}\right)^{\frac{\gamma+1}{\gamma-1}}(1 - P_r^{\frac{1-\gamma}{\gamma}})\right]^{-\frac{1}{2}}$$

where $\gamma = C_P/C_v$ is the ratio of heat capacities at constant pressure and volume.

For convenience, in the following all the thermodynamic quantities are regarded as functions of pressure and entropy, that is,

$$\rho = \rho(P, s), \qquad c^2(P, s) = \left(\frac{\partial P}{\partial \rho}\right)_s, \qquad h = h(P, s)$$

where the entropy s is considered as a constant prescribed parameter.

By virtue of the mass conservation equation, the area ratio A_r can be written as a ratio of momentum at the throat and at the exit of the nozzle, that is, as

$$A_r = \frac{A_2}{A_t} = \frac{\rho_t c_t}{\rho_2 u_2} \tag{2}$$

To compute ρ_t and c_t, the pressure P_t at the throat is needed. By solving the energy equation written at the throat

$$h(P_{01}, s) = h(P_{0t}, s) = h(P_t, s) + \tfrac{1}{2}c^2(P_t, s)$$

for the unkown pressure P_t, we can compute $P_t = P_t(P_{01}, s)$. The momentum at the throat $(\rho c)_t$ is then given by

$$\rho(P_t, s)c(P_t, s), \qquad P_t = P_t(P_{01}, s) \tag{3}$$

and is therefore a function of P_{01} and s only. The exit momentum is finally given by

$$(\rho u)_2 = \rho\left(\frac{P_{01}}{P_r}, s\right)\sqrt{2\left[h(P_{01}, s) - h\left(\frac{P_{01}}{P_r}, s\right)\right]} \tag{4}$$

and is therefore a function of P_r, P_{01}, and s. Because of Eqs. (2–4), the area ratio A_r is also a function of P_r, P_{01}, and s, say

$$A_r = f(P_r, P_{01}, s)$$

The above equation can be iteratively used to obtain the inverse relation

$$P_r = g(A_r, P_{01}, s) \tag{5}$$

All thermodynamic properties are evaluated for entropy $s_{\text{SC1}} = s(P, T) = s$ (18 bar, 304.6°C), using the accurate EoS for MDM [32]. This entropy value is representative for both subcritical and supercritical turbine inlet conditions. The value of the entropy is chosen high enough to avoid condensation during expansion, and representative of typical ORC turbine expansions. The entropy is kept fixed by increasing the inlet total temperature for the higher inlet total pressures. Evaluating Eq. (5) for exit-to-throat area ratios $A_r = [1, 2, \ldots, 10]$, for a range of inlet total pressures $4 \le P_{01} \le 34$ bar and $s = s_{\text{SC1}}$, produces the pressure ratio required for a correctly expanded nozzle as a function of inlet total pressure in the real-gas thermodynamic region of MDM along the specified

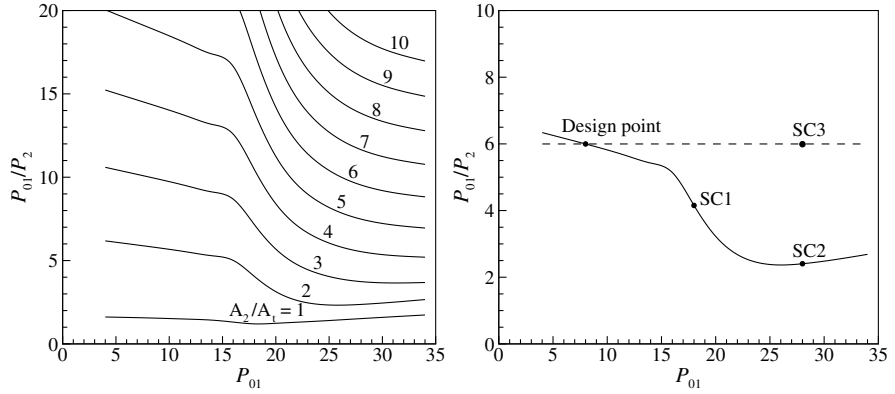

Fig. 3 a) Relation between inlet total pressure and pressure ratio for correctly expanded nozzles in the real-gas thermodynamic region of MDM along isentrope $s = s(P, T) = s$ (8 bar, 270.5°C). Lines denote nozzles that have different exit-to-throat area ratio A_2/A_t. b) Same relation for a correctly expanded nozzle with an exit-to-throat area ratio of $A_2/A_t = 2.04$, which is equal to the stator passage of this study (see Fig. 6a).

isentrope. The relation plotted in Fig. 3a shows that in the nonideal thermodynamic region, as inlet total pressure is increased, for a particular nozzle (with fixed exit-to-throat area ratio), the pressure ratio must be decreased to obtain a correct expansion.

As noticed before, the isentropic transformation based on the ideal-gas law states that the design P_r for a given value of A_r is independent of P_{01}, whereas in the nonideal case P_r decreases as P_{01} increases. This means that for the same inlet total pressure, the ideal-gas case exit pressure $P_{2,\mathrm{id}}$ is lower than the real exit pressure $P_{2,\mathrm{re}}$. If a nozzle operating in nonideal conditions is designed according to the ideal-gas model, that is, if the backpressure is set to $P_{2,\mathrm{id}}$, an overexpansion has to occur at the exit of the nozzle to further expand the gas from the actual exit pressure $P_{2,\mathrm{re}}$ to the lower $P_{2,\mathrm{id}}$. In this case the flow would be overexpanded, and a freejet would be formed downstream of the nozzle, accompanied by strong shock waves which would significantly deteriorate the turbine performance, as shown by the numerical results presented in the next section.

V. Real-Gas Effects in an ORC Stator Blade Passage

The *zFlow* program [24] is employed to demonstrate the effect of inlet total pressure on the two-dimensional flowfield of a real-gas expansion process that typically occurs in ORC nozzles. To this purpose, an existing nozzle geometry has been adopted, even if it has been designed for subcritical inlet conditions for which real-gas effects are mild [41]. The objective is therefore to show that a blade shape specifically designed for supercritical conditions would considerably improve the performance of the stator.

A. Euler Solver

Numerical solutions of the two-dimensional Euler equations are computed with the *zFlow* program [24], linked to the mentioned fluid property library containing several thermodynamic models and a large set of fluid data, including those for the MDM working fluid [27]. All derivatives of thermodynamic properties required by *zFlow* are computed analytically [42]. The main features characterizing the CFD code *zFlow* are briefly summarized. The solver is a hybrid between the finite element and finite volume methods in which the finite volume metric quantities are formulated on the basis of the Lagrangian polynomial shape functions typically used in finite element methods [43]. The spatial approximation of the Euler equations is constructed with a high resolution finite volume method suitable for general unstructured and hybrid grids. The high resolution upwind discretization is constructed on the basis of the Roe approximate Riemann solver [44], generalized to the case of fluids characterized by arbitrary equations of state according to the method of Vinokur and Montagné [45]. This class of discretization schemes is particularly well suited to the computation of high Mach number flows such as those occurring in an ORC turbine. The use of unstructured grids allows for the straightforward treatment of domains of arbitrarily complex geometry. Another important feature of *zFlow* is represented by the adopted implicit time-integration scheme, which computes steady-state solutions in a much more efficient way with respect to conventional explicit schemes [24]. The gain in computational efficiency is crucial when complex EoS are needed for an accurate flow simulation. The *zFlow* solver has been already successfully validated for ideal-gas simulations [24,46]. To the knowledge of the authors no experimental data of organic flows in the so-called real-gas thermodynamic region are available. An experimental setup aimed at gas dynamic measurements of these type of flows is therefore planned. The extension of *zFlow* to the viscous Reynolds-averaged Navier–Stokes equations will be published soon.

B. Validation: Recovery of Ideal-Gas Results Around the VKI LS-89 Blade

Validation of the *zFlow* solver for dense-gas flows in turbine cascades is currently not possible due to the mentioned lack of experimental data. For the moment, the best alternative is to validate the *zFlow* code linked to the mentioned fluid property library containing the MPEoSs for a turbomachinery test case that describes several expansions occurring in the thermodynamic region where the ideal-gas law would apply.

The results of simulations are thus compared to the measurements of two well-known and reliable turbomachinery test cases [47] for dry air at ideal-gas conditions. In both test cases, the geometry is the VKI LS-89 blade, which is a standard high pressure turbine nozzle guide vane, mounted in a linear cascade. The first test case (MUR-43) is at subsonic flow conditions ($Ma_{\mathrm{is}} < 0.84$), and the second test case (MUR-49) at transonic flow conditions ($Ma_{\mathrm{is}} < 1.02$). The conditions are given in Table 3.

For the prediction of the thermodynamic properties of air a 19-parameter EoS [48] is used.

The periodic grid is generated in a transformed domain, in which periodic boundaries are mapped into internal curves to simplify the task of obtaining periodic nodes [49]. In the transformed space the grid is generated by the front-advancing/Delaunay method [50] and then transformed back into the physical space of XY coordinates by introducing a suitable cut. This translates into the sawlike edge of the periodic boundaries shown in Fig. 4.

Table 3 Test case conditions from [47]

		MUR43	MUR49
Total inlet pressure	P_{01}, bar	1.435	1.608
Expansion ratio	P_{01}/P_2, −	1.587	1.938
Total inlet temperature	T_{01}, °C	146.85	146.85
Compressibility factor at inlet	Z_1, −	1	1
Static outlet pressure	P_2, bar	1.333	2
Isentropic Mach number at outlet	$Ma_{2,\mathrm{is}}$, −	0.84	1.02

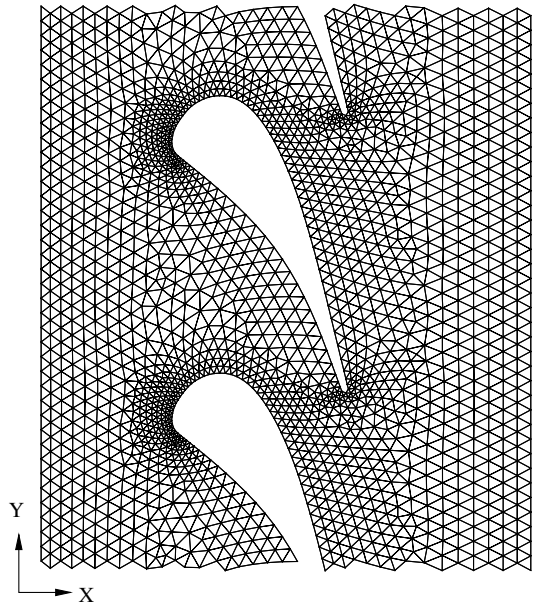

Fig. 4 Cascade of two stacked coarse grids.

All flow solutions have converged up to at least a reduction of 5 orders of magnitude measured in the L^2 norm of the conserved variables. The numerical solution of the Mach number distribution along the blade surface is compared to the experimental data of the test cases.

To determine the discretization error level, a grid convergence study is performed by computing the solution on three increasingly finer grids using the accurate MPEoS. The fine grid and the coarse grid are generated by, respectively, halving and doubling the number of grid elements with respect to the initial medium grid. The coarse grid consists of 1302 nodes and 2032 elements, the medium grid of 2383 nodes and 3958 elements, and the fine grid of 4153 nodes and 7184 elements. Figure 4 shows the coarse grid and the blade geometry. The lines in Figs. 5a and 5b show the Mach number distributions for the MUR43 and MUR49 test cases, respectively, solved on the coarse, medium, and fine grids. They are plotted as a function of the coordinate reduced with the axial blade chord, X/C_{ax}. From the results, it appears that the solution computed using the fine grid is grid independent.

The *zFlow* code is validated for this transonic fluid-dynamic problem by comparing the numerical solution to the experimental data of the test case, given in [47]. The static pressure measurement data have an uncertainty of 0.5%, leading to uncertainties in the isentropic Mach number as indicated by the error bars in Fig. 5. The comparison pertaining to the subsonic test case MUR43, shown in Fig. 5a, shows very good agreement between numerical and experimental results. For the transonic test case MUR49, shown in Fig. 5b, the agreement is good. The location of the shock wave that terminates the supersonic region is predicted by *zFlow* at the end of the blade profile ($X/C_{\mathrm{ax}} = 0.95$), whereas the measurements indicate that the shock wave is further upstream ($X/C_{\mathrm{ax}} = 0.88$). Still, the difference is small and the agreement is good enough.

C. ORC Stator Blade Passage

The flowfield through the two-dimensional axial stator nozzle of an existing ORC turbine operated with the siloxane MDM as a working fluid is chosen as a practical example. Three cases are considered: the design point of the existing turbine stator, part-load operation, and operation at supercritical pressures. The turbine operating conditions of each case, which are also the prescribed boundary conditions in the simulations (except for the compressibility factor), are given in Table 4. The expansions are given in the temperature-entropy diagram in Fig. 6b. The inlet conditions of all flow simulations presented in this paper lie on the same isentrope as indicated in the quasi-one-dimensional isentropic flow analysis of Sec. IV. The entropy is kept fixed by increasing the inlet total temperature for higher inlet total pressures.

The passage, as shown in Fig. 6a, has been designed without the use of an accurate two-dimensional real-gas CFD simulation tool, as this was not available at the time of the design. Instead, its design is based on the contour of a 1-D nozzle. It is essentially the bottom part of a converging–diverging nozzle that has been curved to obtain the desired stator outflow angle. It should be noted that in the figures, the aspect ratio is distorted, because the turbine design is confidential property of the manufacturer. The throat area A_t and exit area A_2 in a turbine passage are defined as shown in Fig. 6a. For the current passage, the exit-to-throat area ratio was determined to be $A_2/A_t = 2.04$, where the passage is assumed to be rectangular so that the area ratio equals the length ratio.

The accurate multiparameter EoS by Span and Wagner discussed in Sec. III is used as a thermodynamic model. In practice, the polytropic ideal-gas (PIG) law is often adopted for the design of turbines. In ORC nozzles, however, the fluid flow is in nonideal thermodynamic conditions, so that the PIG model is not fully justified. Under supercritical conditions, the associated errors are even larger. To demonstrate the relevance of this error in the calculation of the fluid-dynamic parameters, the fluid-dynamic simulations are also computed based on the PIG model. The PIG model is given by $P = RT/v$. The specific gas constant is defined as $R = \mathcal{R}/M$, where the universal gas constant is $\mathcal{R} = 8.314\ \mathrm{J/(mol \cdot K)}$. The other necessary information for the calculation of all caloric properties is the ideal-gas specific heat at constant pressure which is $C_P^0 = \gamma R/(\gamma - 1)$. For the PIG model, a constant ratio of specific heats of $\gamma = 1.01733$ is adopted, which is calculated from the isobaric and isochoric ideal-gas specific heats evaluated at the critical temperature, as this characteristic temperature is, in this case, close to the turbine inlet temperature (cf. Table 4). Evaluating the specific heat ratio at an intermediate

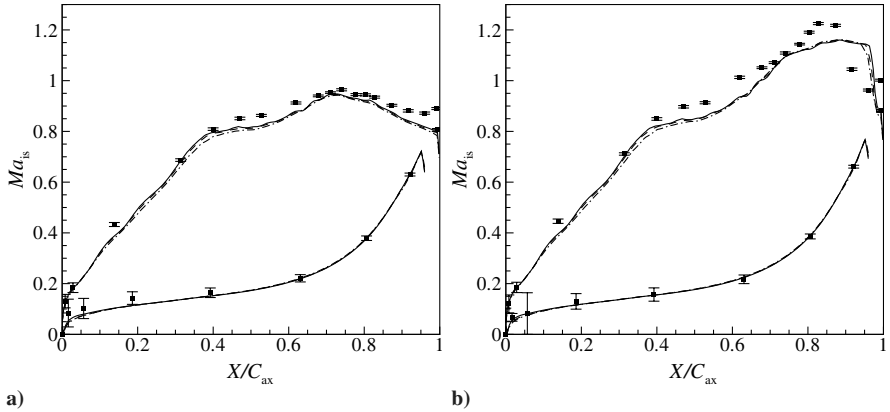

Fig. 5 Mach number distribution for the MUR43 test case a) and the MUR49 test case b). Shown are the experimental measurements (■) from [47] and the numerical solution on the coarse grid (dash-dotted lines), the medium grid (dashed lines), and the fine grid (solid lines).

Table 4 Turbine stator operating conditions for the the geometry of Fig. 6a

		Design point	Part load	SC1	SC2	SC3
Pressure ratio	P_{01}/P_2, –	6	4	4.15	2.40	6
Inlet total pressure	P_{01}, bar	8	8	18	28	28
Inlet total temperature	T_{01}, °C	270.5	270.5	304.6	311.1	311.1
Inlet compressibility factor	Z_{01}, –	0.72	0.72	0.26	0.32	0.32
Outlet static pressure	P_2, bar	1.33	2	4.33	11.65	4.67
Outlet compressibility factor	Z_2, –	0.96	0.93	0.86	0.55	0.85

temperature between the inlet and the outlet temperature does not alter the results, as the change in γ is almost nonappreciable (from 1.01733 to 1.01795 at most).

The periodic computational grid is generated using the same procedure as described in Sec. V.B. A grid convergence study was conducted to ensure that the solution was grid independent [41].

The "best practice" solution procedure involves starting from a uniformly distributed initial flowfield. Starting from a flowfield solution of a similar problem, if available, is preferred as it reduces the number of iterations. This strategy is even mandatory for the simulation of problems with high expansion ratios, which do not converge if started from a uniformly distributed initial flowfield. An optimal convergence rate is obtained using the implicit backward Euler time-integration scheme, starting with a standard outflow boundary condition and a low Courant–-Friedrichs–Lewy (CFL) number for the initial 10 iterations to avoid computational blowup. Subsequently, the more realistic nonreflecting version of the outflow boundary condition is adopted [51] and, to allow for very large pseudotime steps, the CFL number is automatically increased as the solution converges [24]. All flow solutions are converged up to at least 6 orders of magnitude measured in the L_2 norm of all the conserved variables.

It should be noted that the Euler solver used in this work permits one to investigate the main inviscid features of the flowfield through the stator passage, which are the focus of this paper. Viscous phenomena such as boundary layers and a turbulent wake, which are present in the real flowfield, cannot be taken into account yet.

D. Design-Point Simulation

The stator blade passage has been designed both in terms of expansion ratio and two-dimensional shape for the design-point operating conditions as reported in Table 4.

The compressibility factor, defined as $Z = Pv/RT$, is identically equal to unity for an ideal gas; it is therefore often used to quantify the nonideality of the thermodynamic state. As indicated by the values of the compressibility factor at the inlet and the outlet of the nozzle given in Table 4, only a limited portion of the expansion through this turbine stator passage occurs in the nonideal gas thermodynamic region. This might be due to the fact that a lack of real-gas CFD simulation tools such as *zFlow* has limited the design of ORC turbines operating at thermodynamic conditions that deviate further from ideality, even if they might be more thermodynamically favorable.

Figure 7a shows the computed flowfield based on the accurate SW EoS visualized by equidistant iso-Mach lines and streamlines. From the inflow boundary on the left-hand side of the domain, the fluid accelerates through the passage formed by the stator blade cascade to supersonic velocities. At the blade trailing edge, a small region of slight overexpansion can be observed in the iso-Mach line plot. Further downstream, the flow appears to be slightly overexpanded, as it is bent slightly into itself resulting in a very weak oblique shock. Nonetheless, some weak shocks are unavoidable in this curved geometry and the blade passage appears to be reasonably well designed for the specified (design-point) pressure ratio.

Figure 8 shows the blade surface distributions of isentropic Mach number, pressure coefficient, speed of sound, velocity, density, and compressibility factor. To clearly visualize parameter changes also for the rear part of this high-turning blade, the distributions are plotted as a function of the reduced coordinate S/C, starting from the leading edge defined by $X/C_{\text{ax}} = 0$. To show the effect of the thermodynamic nonideality on the blade surface distributions, the distributions computed based on the ideal-gas law are shown in the same figure. It is noted that for design-point and part-load conditions this nonideality is relatively mild (see Table 4).

The isentropic Mach number distribution is given in Fig. 8a. The line that indicates early expansion (with a maximum in the Mach number) pertains to the suction side of the blade, the line with retarded expansion ending at $S/C = 0.92$ to the pressure side. The isentropic Mach number distribution of the suction side does not vary smoothly at the location $S/C = 0.52$–0.6, indicating irregular expansion. More important, there exists a high peak at $S/C = 0.92$ on the suction side, corresponding to the point of impingement of the weak oblique shock emanating from the trailing edge of the top blade of the passage. This shock wave recompresses the flow downstream, which is detrimental to the desired continuous and smooth expansion along the entire blade surface. In the real viscous case and depending on the Reynolds number, the adverse pressure gradient may introduce the risk of boundary-layer separation and associated increase in losses. In this study, this loss mechanism cannot be taken

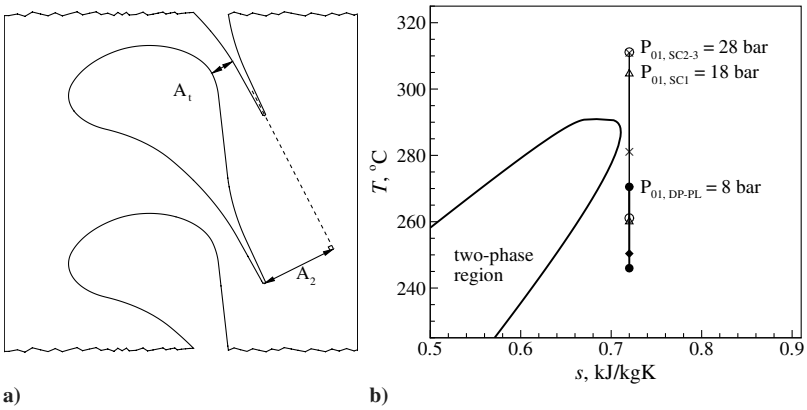

a) b)

Fig. 6 a) Definition of throat area A_t and exit area A_2 in the turbine blade passage. This passage has an exit-to-throat area ratio of $A_2/A_t = 2.04$. The figure aspect ratio is deformed, because the blade design is confidential property of the manufacturer. b) Simulated expansions in the temperature-entropy diagram of MDM: Design point (● and thick line), part load (◆), SC1 (△), SC2 (×), SC3 (○).

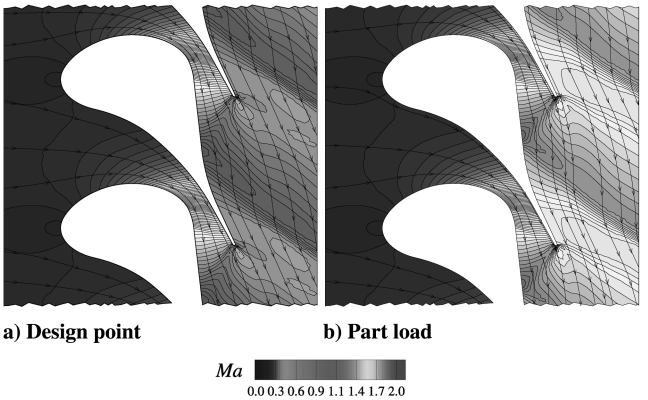

Fig. 7 Flowfields (iso-Mach and streamlines) at design-point and part-load operation. Operating conditions are given in Table 4.

into account. Nonetheless, it is evident that there is room for improvement in the design of this blade. The isentropic Mach number distribution based on the ideal-gas law appears quite similar to the isentropic Mach number distribution based on the accurate SW EoS. Nonetheless, the isentropic Mach number according to PIG is 10% lower at the leading edge ($S/C = 0$), where the nonideality is higher as indicated by the compressibility factor in Fig. 8f. The initial high nonideality has, however, little effect on the absolute value of the isentropic Mach number because the latter is initially very low. Further downstream, at $S/C \approx 0.7$ on the suction side as well as at $S/C \approx 0.9$ on the pressure side, the isentropic Mach number based on the PIG EoS is 5% higher.

The distribution of the pressure coefficient defined as

$$C_P \equiv \frac{P_{01} - P}{P_{01} - P_2} \tag{6}$$

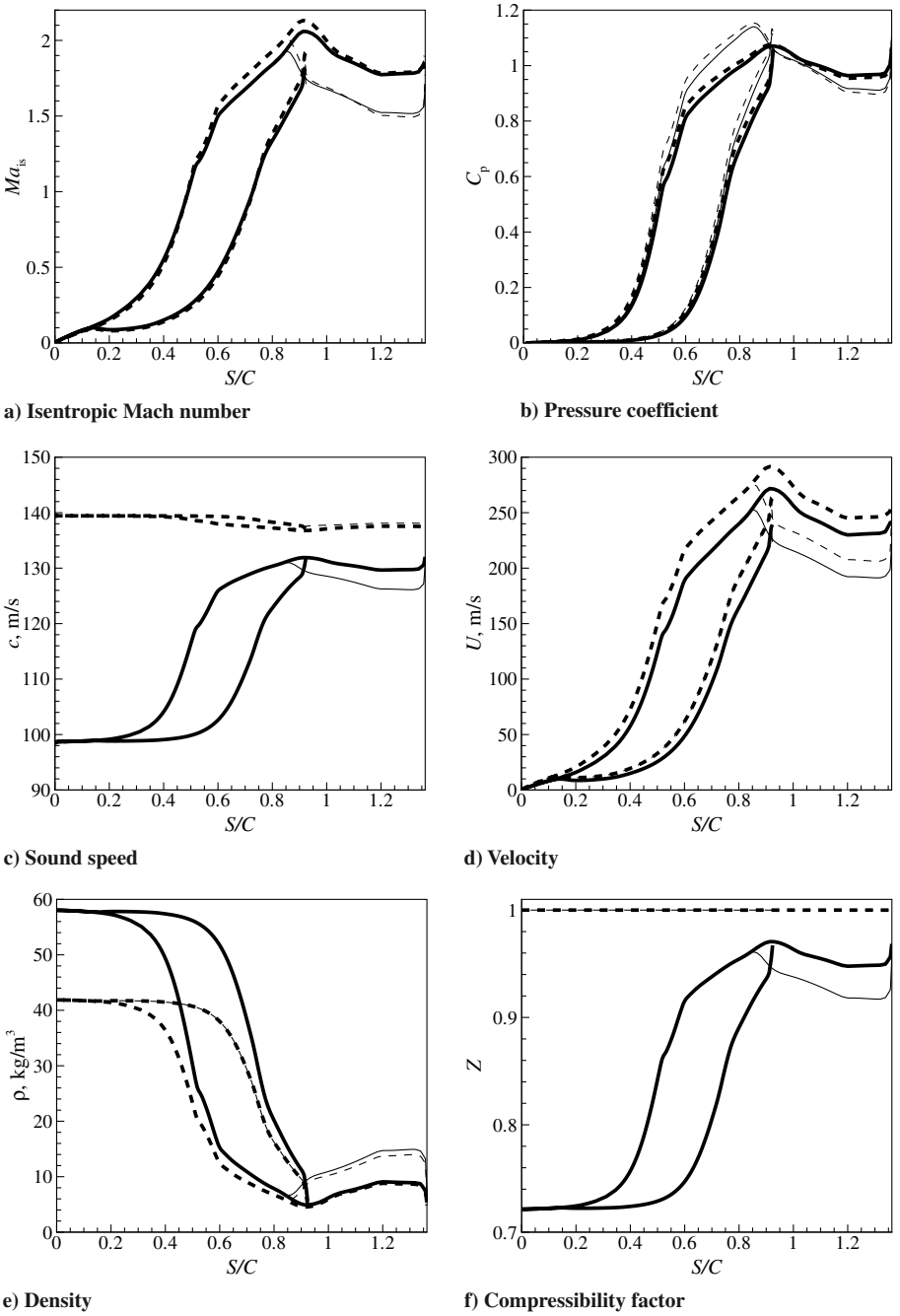

Fig. 8 Blade surface distributions at design point (thick lines) and part load (thin lines) based on the accurate SW EoS (solid lines) and on the PIG EoS (dashed lines). Operating conditions are given in Table 4.

Table 5 Performance parameter differences between EoSs and between stator operating points

	$\Delta\dot{m}$, %	ΔC_{PL}, %
a) Percentage difference of the mass flow rate ($\Delta\dot{m}$) and pressure loss coefficient (ΔC_{PL}, where $C_{PL} \equiv 1 - P_{02}/P_{01}$) based on the PIG model with respect to the accurate values based on the SW EoS, for the indicated operating condition.		
Design point	−6	−3
Part load	−6	6
SC1	−24	−13
SC2	−50	1100
SC3	−50	−79
b) Percentage difference of the mass flow rate ($\Delta\dot{m}$) and pressure loss coefficient (ΔC_{PL}) with respect to design-point values, for the part-load and supercritical cases analyzed in this work.		
Design point	0	0
Part load	0	41
SC1	171	61
SC2	533	−63
SC3	533	354

is shown in Fig. 8b. Its trend is similar to the one of the isentropic Mach number.

The sound speed is shown in Fig. 8b. Because the inlet state is relatively close to the critical point, the speed of sound is initially low ($c = 93$ m/s), but increases considerably as the fluid expands, ultimately reaching a value of $c \approx 128$ m/s. Such an increase in sound speed across an isentropic expansion can occur only for molecularly complex fluids within a certain thermodynamic region [52]. The PIG model incorrectly predicts a 48% higher initial sound speed ($c \approx 137$ m/s) which decreases only slightly during expansion, which, under ideal-gas theory, is always the case for an isentropic expansion.

The trend of the velocity magnitude, shown in Fig. 8d, is also similar to that of the isentropic Mach number. Similar to what is observed for the isentropic Mach number, the PIG model incorrectly predicts higher values for the velocity, the maximum error being 35%. This explains the relatively limited error in isentropic Mach number of only 10%.

Density at the blade leading edge is high, but decreases as the fluid expands into the dilute ideal-gas region. Because pressure and temperature are the prescribed variables at inflow and outflow, the density depends on the EoS model. The density resulting from the computation based on PIG is initially 30% lower, but this difference monotonically decreases to 3% along the rear part of the blade, as the fluid expands toward lower pressure (ideal-gas) states.

Although based on the PIG model the velocities are higher, the densities are much lower, thus partially compensating each other but resulting in a net 6% lower mass flow rate if compared to the SW EoS (see Table 5a).

The distribution of the compressibility factor shown in Fig. 8f expresses the deviation from the ideal-gas law. This nozzle has been designed for inlet conditions corresponding to a slightly superheated vapor at a reduced pressure $P_{01}/P_{cr} \approx 0.56$, with a large pressure ratio so that the process evolves very rapidly toward lower pressure states (near ideal gas). Indeed the distribution of the compressibility factor confirms that only in the initial phase of the expansion through the blade nozzle (i.e., only along the first half of the blade surface) in both the design-point and part-load cases, the flow is thermodynamically nonideal. Significant real-gas effects are therefore present only in this initial region. The predicted performance of the nozzle blade in design conditions is therefore not heavily affected by the chosen thermodynamic model even if some differences have indeed been proven.

E. Part-Load Simulation

Because ORCs can operate at part-load conditions, the associated performance is important. To get an idea of the changes in the flowfield and possible deterioration of the performance, part-load simulations are carried out. It is assumed that for part-load operation, the total pressure at the inlet is controlled to remain at $P_{01} = 8$ bar. This can be accomplished, for example, by partial-arc admission. In this particular part-load condition, the pressure ratio, P_2/P_{01}, is reduced from 6 to 4, so that the backpressure is higher (see Table 4).

The computation using the accurate SW EoS is again used to investigate the flowfield of the expansion process. Figure 7b shows the computed flowfield visualized by equidistant iso-Mach lines and streamlines. As shown in the figure, at part-load operation the flow becomes overexpanded halfway along the blade suction surface and the weak oblique shock becomes stronger. Indeed, the pressure loss is 41% higher in comparison to design-point operation.

The surface distributions at part load are plotted in Fig. 8. Here, thin lines pertain to part-load distributions. It can be observed that in all blade distributions the initial part ($S/C < 0.75$) is the same for design point and part load, because the stator nozzle is choked (this is confirmed by the mass flow rate being equal to that of the design point, as shown in Table 5b). An exception is the pressure coefficient (Fig. 8b), because its definition, given by Eq. (1), depends on the outlet pressure P_2. The difference with respect to design-point operation is that because the pressure ratio is reduced, first, the isentropic Mach number after expansion is lower (Fig. 8a) and, second, the outflow pressure is higher so that the final part of the expansion occurs in the nonideal thermodynamic region for a larger portion (see Fig. 8f). This leads to a larger deviation of sound speed, velocity magnitude, and density if the PIG model is compared to the SW model. In part-load conditions, the PIG EoS predicts 6% stronger shock waves if compared to the accurate SW EoS, as indicated by the pressure loss coefficient given in Table 5a. The pressure loss coefficient is defined as the mass-weighted average over the outflow boundary of $C_{PL} \equiv 1 - P_{02}/P_{01}$.

F. Supercritical Simulations

Flow simulations at supercritical inlet pressures are performed to demonstrate the effect of supercritical inlet total pressures on the two-dimensional flowfield of the expansion process and the required reduction pressure ratio to obtain correctly expanded flow.

Three supercritical operating conditions are considered, indicated by SC1, SC2, and SC3 in Table 4. SC1 and SC2 represent two possible operating conditions at moderate and high inlet total pressure that are above the critical pressure: $P_{01}/P_{cr} = 1.27$ and 1.98, respectively. To obtain correctly expanded flow, the pressure ratios of SC1 and SC2 are decreased according to the real-gas quasi-one-dimensional flow analysis of Sec. IV as shown in Fig. 3b, so that $P_{01}/P_2 = 4.15$ and 2.40, respectively. The SC3 case has an inlet total pressure equal to the SC2 case ($P_{01}/P_{cr} = 1.98$), but the pressure ratio is deliberately not set according to the results of the real-gas quasi-one-dimensional flow analysis, but according to the PIG model which means a pressure ratio equal to the design point ($P_{01}/P_2 = 6$), as indicated in Fig. 3b. The resulting expansion cases are also given in the temperature-entropy diagram in Fig. 6b.

Figure 9 shows the computed flowfields of the supercritical cases visualized by equidistant iso-Mach lines and streamlines. The SC1 and SC2 cases show a correctly expanded flowfield, without the

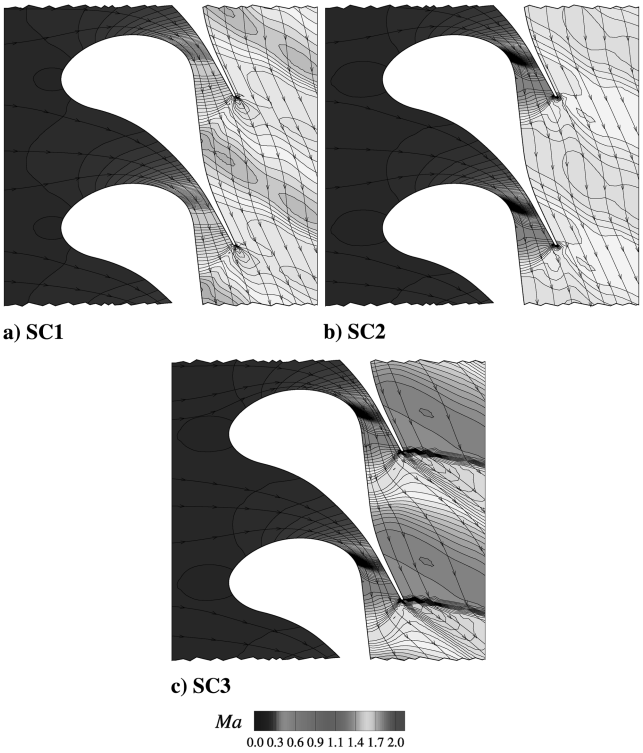

Fig. 9 Flowfields (iso-Mach and streamlines) at supercritical operation. Operating conditions are given in Table 4.

formation of shocks. This confirms the correctness of the relation between inlet total pressure and pressure ratio. In fact, the flowfield of the SC2 case (Fig. 9b) appears to have a more uniform Mach distribution, indicating that the very weak oblique shock that is present even in the design-point flowfield is absent in the SC2 case. This is confirmed by the pressure loss coefficient (Table 5b), which is 63% lower in comparison to its value at the design point. This again puts in evidence the fact that it may be possible to further improve the design of the stator for design-point conditions. Another important result is that the use of a blade geometry designed for subcritical operating conditions would lead to rather unsatisfactory Mach numbers and pressure coefficient distributions along the blade (Fig. 9c), if employed for nozzles expanding from supercritical inlet conditions. These Mach number and pressure distributions may suggest the deterioration of the turbine performance.

The SC3 case shows highly underexpanded flow as it exits the stator passage, as was expected from the results of the real-gas quasi-one-dimensional flow analysis in Sec. IV. Even after having undergone the expansion process in the stator passage, the pressure at the exit is still considerably higher than the backpressure, so that the flow expands further in a freejet that is formed downstream of the stage, as indicated in Fig. 9c by the distinct slip line originating from the trailing edge. The means for further expansion is provided for by an expansion fan that originates from the trailing edge and extends inwardly. Further downstream, at the other side of the blade trailing edge, the flow is subjected to a strong shock wave. Consequently, the pressure loss coefficient is 354% higher in comparison to the design-point value (see Table 5b). This undesirable flowfield would be the result if an ORC turbine stage that is intended to operate at supercritical pressures were designed based on computations that employ the ideal-gas law.

The SC3 case is also computed based on the PIG model and compared to the design-point computation based on the PIG model. As expected, the two flowfields, shown in Fig. 10, are identical. This shows, as is well known, that under the PIG model the flowfield of the expansion process is not dependent on inlet total pressure, but only on static outlet-to-total inlet pressure ratio. A comparison between the PIG and SW EoS for the design-point case has already been given in Sec. V.D.

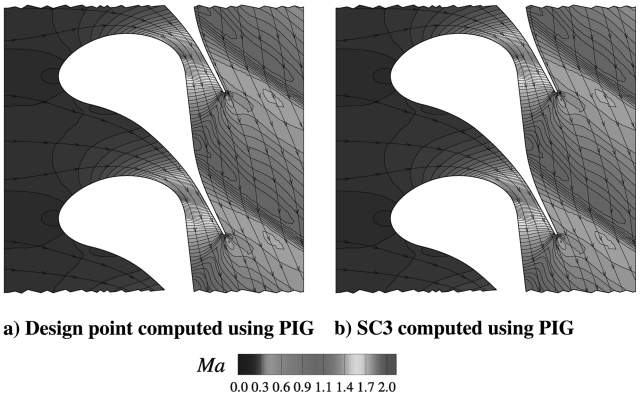

Fig. 10 Flowfields (iso-Mach and streamlines) computed using the PIG model. Operating conditions are given in Table 4.

The blade distributions of the relevant parameters show more clearly the real-gas effects occurring at supercritical pressures. They are plotted for the three supercritical cases SC1, SC2, and SC3. The distributions for the design point are included to serve as a basis for comparison.

The Mach number is necessarily equal to unity at the throat for all cases; therefore the isentropic Mach number distribution along the blade surface, shown in Fig. 11a, shows a similar trend for all cases. For higher pressures (increasing from design point to SC1 and further to SC2), the subsonic isentropic Mach number upstream of the throat is lower. The isentropic Mach number indicates that, in the moderately supercritical case SC1, expansion is absent for some length just downstream of the throat but then continues similarly to the design-point case. For the highly supercritical cases SC2 and SC3, the expansion occurs very rapidly at the throat. For the SC3 case, the freejet provides further expansion from $S/C = 0.85$ onward. The pressure coefficients in Fig. 11b show similar trends for all cases, except for SC3 where the freejet expansion is clearly visible.

The speed of sound has a minimum at the thermodynamic critical point. For supercritical expansions, the speed of sound decreases and has a minimum ($c = 49.2$ m/s) where the critical pressure is crossed. This can be observed in Fig. 11c. It also shows large variations in speed of sound during expansion in the three supercritical cases. The SC1 case, being closest to the critical point, has the lowest inlet speed of sound; the SC2 and SC3 cases, being highly supercritical, have a very high speed of sound at the inlet. Their speed of sound shows a strong decrease, followed by a strong increase, which is even larger than the increase in the velocity magnitude (Fig. 11d), leading to a decreasing isentropic Mach number (Fig. 11a for $0.6 < S/C < 0.8$) during expansion (cf. Fig. 11b). This phenomenon is discussed in more detail in [53].

The velocity magnitude, shown in Fig. 11d, is considerably lower for all supercritical cases if compared to the design-point case. This is because the pressure ratio is lower for the SC1 and SC2 cases, which corresponds to a lower enthalpy drop and therefore lower velocities. In the SC3 case (which has a pressure ratio equal to the design point), the reduction in enthalpy drop with respect to the design point is still present, though not as large. In this case, the reduction in enthalpy drop is due to real-gas thermodynamic behavior at these nonideal conditions; the enthalpy drop becomes smaller as inlet pressure is increased at constant pressure ratio.

Along a given isentrope, density increases as pressure is increased, resulting in the high compressibility for supercritical states. Indeed, it can be observed in Fig. 11e that the densities of the moderately supercritical case SC1 are much higher in comparison to the design point. This is even more so for the highly supercritical cases SC2 and SC3. Volumetric expansion ratios of 7.8, 12.9, and 4.1 are observed for the cases design points, SC1 and SC2, respectively.

Even though the velocity is only slightly lower, the density is much higher for the supercritical cases (higher compressibility), resulting in a mass flow rate that is much higher in comparison to the

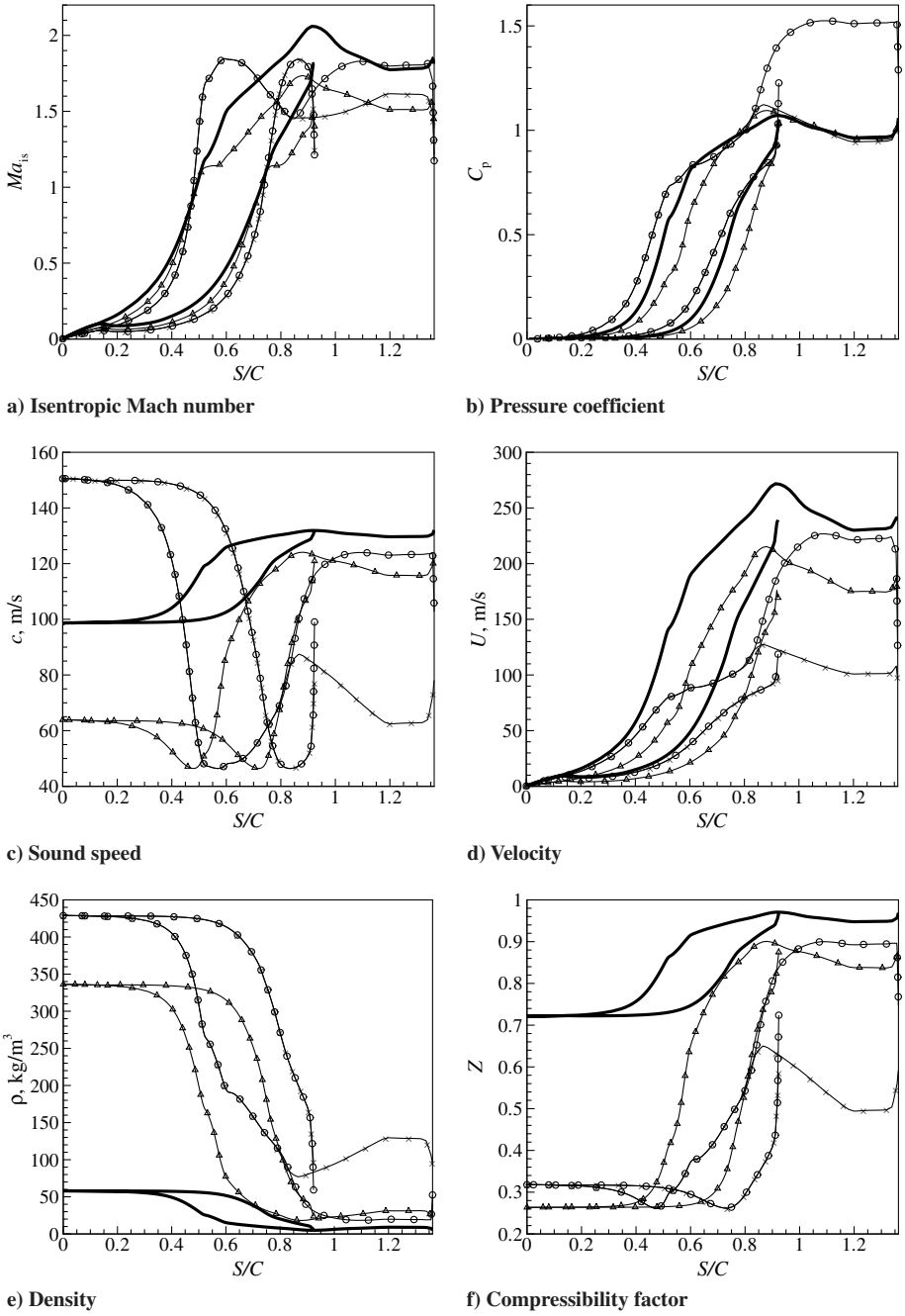

Fig. 11 Blade surface distributions of design-point and SC cases. Design point (thick line), SC1 (△), SC2 (×), and SC3 (○).

design point: a factor 1.7 and 5.3 higher for SC1 and SC2/SC3, respectively (see Table 5b).

The compressibility factor, shown in Fig. 11f, shows that the supercritical cases deviate from the PIG law in terms of thermal behavior far more than for the design-point case. The initial deviations are as high as 74 and 68% for SC1 and SC2, respectively. After the critical pressure has been crossed, the nonideality is reduced to less than 20% (SC1) and 50% (SC2).

VI. Conclusions

This paper presents an investigation on real-gas effects in ORC nozzle flows for inlet conditions at sub- and supercritical pressures. It is known that supercritical ORCs are thermodynamically more efficient; however, they are not yet adopted in practice. One of the reasons is that suitable tools for the fluid-dynamic design of the turbine geometry operating at supercritical conditions have not been available until recently.

The first part of the investigation is based on a quasi-one-dimensional isentropic nozzle analysis (the first step in the design of any nozzle) employing an accurate thermodynamic model. It shows that the pressure ratio needs to be significantly reduced to obtain efficient expansion if the same stator nozzle is to be used or, reversely, a nozzle geometry with a much higher exit-to-throat area ratio is required to obtain an efficient expansion at supercritical pressures.

In the second part, real-gas two-dimensional inviscid fluid-dynamic simulations of an actual ORC stator blade cascade with siloxane MDM as working fluid have been carried out for five different operating conditions. The flow simulations are performed with the CFD code *zFlow*, which is linked to a library containing accurate thermodynamic models. The validation of *zFlow* on the well-known test case of the VKI LS-89 transonic turbine blade shows good agreement with experimental data. The subsequently analyzed cases of the ORC stator blade cascade include a simulation of the flow in design and part-load conditions and three simulations of expansions starting at supercritical inlet pressures.

The results, illustrated by two-dimensional flowfields (distributions of relevant flow variables along the blade surface and two integral performance parameters), show the aforementioned real-gas effect in more detail. Moreover, the results show additional real-gas effects in the supercritical expansions such as the low speed of sound and low velocity as compared to design-point conditions. Furthermore, the supercritical expansions are characterized by very high densities and mass flow rates.

The results obtained for the supercritical cases show that the significant nonideal flow effects lead to rather unsatisfactory Mach numbers and pressure coefficient distributions along the blade which may substantially deteriorate the turbine performance. This demonstrates that standard design methods are not well suited to obtain a proper design in strongly nonideal thermodynamic regions, and that in such flow conditions CFD simulations employing accurate thermodynamic models could lead to a significantly improved design.

Future work will focus on the extension of the analysis by means of Navier–Stokes simulations (to take into account viscous losses and shock-induced boundary-layer separation) and blade shape optimization to demonstrate improved performance.

Acknowledgments

This research is supported by the Dutch Technology Foundation STW, applied science division of the Netherlands Organization for Scientific Research (NWO), the Technology Program of the Ministry of Economic Affairs, and the Delft Centre for Sustainable Industrial Processes. The authors are grateful to Turboden srl for providing data of an existing ORC plant and for many interesting discussions.

References

[1] Curran, H., "Use of Organic Working Fluids in Rankine Engines," *Journal of Energy*, Vol. 5, No. 4, 1981, pp. 218–223.

[2] Angelino, G., Gaia, M., and Macchi, E., "A Review of Italian Activity in the Field of Organic Rankine Cycles," *VDI Berichte—Proceedings of the International VDI-Seminar*, Vol. 539, VDI, VDI Verlag Düsseldorf, 1984, pp. 465–482.

[3] Colonna, P., "Fluidi di Lavoro Multi Componenti Per Cicli Termodinamici di Potenza (Multicomponent Working Fluids for Power Cycles)," Ph.D. Thesis, Politecnico di Milano, Milano, Italy, Oct. 1996.

[4] Hung, T. C., "Waste Heat Recovery of Organic Rankine Cycle Using Dry Fluids," *Energy Conversion and Management*, Vol. 42, No. 5, 2001, pp. 539–553. doi:10.1016/S0196-8904(00)00081-9

[5] Boretz, J. E., "SuperCritical Organic Rankine Engines (SCORE)," *IECEC '86: Proceedings of the Twenty-First Intersociety Energy Conversion Engineering Conference*, American Chemical Society, Washington, D.C., 1986, pp. 2050–2054.

[6] Yamamoto, T., Furuhata, T., and Arai, N., "Design and Testing of the ORC," *Energy*, Vol. 26, No. 3, 2001, pp. 239–251. doi:10.1016/S0360-5442(00)00063-3

[7] Bronicki, L. Y., "Electrical Power from Moderated Temperature Geothermal Sources with Modular Mini-Power Plants," *Geothermics*, Vol. 17, No. 1, 1988, pp. 83–92. doi:10.1016/0375-6505(88)90007-7

[8] Kutscher, C., "The Status and Future of Geothermal Electric Power," *American Solar Energy Society (ASES) Conference*, NREL/CP-550-28204, National Renewable Energy Laboratory (NREL), 2000.

[9] Bertani, R., "What is Geothermal Potential?," *International Geothermal Association News*, Vol. 53, July 2003, pp. 1–3.

[10] Obernberger, I., Thonhofer, P., and Reisenhofer, E., "Description and Evaluation of the New 1000 kW ORC Process Integrated in the Biomass CHP Plant in Lienz, Austria," *Euroheat and Power*, Vol. 10, No. 1, 2002, pp. 1–17.

[11] Savola, T., Fogelholm, C. J., and Keppo, I., "Small-Scale Biomass CHP Plant and District Heating," Helsinki University of Technology, VTT Research Notes 2301, Helsinki, Finland, 2005.

[12] Hassani, V., and Price, H. W., "Modular Trough Power Plants," Tech. Rept. NREL/TP-550-31240, National Renewable Energy Laboratory, 2001.

[13] Angelino, G., and Colonna, P., "Organic Rankine Cycles for Energy Recovery from Molten Carbonate Fuel Cells," *Proceedings of the 35th Intersociety Energy Coversion Engineering Conference (IECEC)*, AIAA, Reston, VA, 24–28 July 2000, pp. 1400–1409.

[14] Angelino, G., and Colonna, P., "Air Cooled Siloxane Bottoming Cycle for Molten Carbonate Fuel Cells," *Proceedings of the 2000 Fuel Cell Seminar*, Courtesy Associates, Washington, D.C., 30 Oct. – 2 Nov. 2000, pp. 667–670.

[15] Chaudoir, D. W., Niggeman, R. E., and Bland, T. J., "A Solar Dynamic ORC Power System for Space Station Application," *Proceedings of the 20th IECEC*, 859085, Society for Automotive Engineers, Warrendale, PA, 1985, pp. 1.58–1.65.

[16] Angelino, G., and Invernizzi, C., "Cyclic Methylsiloxanes as Working Fluids for Space Power Cycles," *Journal of Solar Energy Engineering, Transactions of the ASME*, Vol. 115, No. 3, 1993, pp. 130–137.

[17] Heidenreich, G., Bland, T., and Niggemann, R., "Receiver for Solar Dynamic Organic Rankine Cycle (ORC) Powered Space Station," *Proceedings of the 20th IECEC*, 859220, Society for Automotive Engineers, Warrendale, PA, 1985, pp. 1.228–1.245.

[18] Cole, R. L., Demirgian J. C., and Allen, J. W., "Predicting Toluene Degradation in Organic Rankine Cycle Engines," *Proceedings of the 22nd IECEC*, 879075, AIAA, New York, 1987, pp. 1–8.

[19] Havens, V. N., Ragaller, D. R., and Namkoong, D., "Solar Dynamic Organic Rankine Cycle Heat Rejection System Simulation," *Proceedings of the 22nd IECEC*, 879284, AIAA, New York, 1987, pp. 222–226.

[20] Boyle, R. V., Coombs, M. G., and Kudija, C. T., "Solar Dynamic Power Option for the Space Station," *Proceedings of the 23rd IECEC*, 889163, ASME, New York, 1988, pp. 319–328.

[21] Blumenberg, J., and Ruppe, H. O., "Comparison of Nuclear and Solar Power Plants with Turboelectric Generations for Application in Space," *Acta Astronautica*, Vol. 12, No. 5, 1985, pp. 293–307. doi:10.1016/0094-5765(85)90064-5

[22] Meier, K. L., Kirchner, W. L., and Willcut, G. J., "Compact Reactor/ORC Power Source," *Intersociety Energy Conversion Engineering Conference*, American Chemical Society, Washington, D.C., 25 Aug. 1986, pp. 1–7.

[23] Brown, B. P., and Argrow, B. M., "Application of Bethe-Zel'dovic-Thompson Fluids in Organic Rankine Cycle Engines," *Journal of Propulsion and Power*, Vol. 16, No. 6, Nov.–Dec. 2000, pp. 1118–1123.

[24] Colonna, P., and Rebay, S., "Numerical Simulation of Dense Gas Flows on Unstructured Grids with an Implicit High Resolution Upwind Euler Solver," *International Journal of Numerical Methods Fluids*, Vol. 46, No. 7, 2004, pp. 735–765. doi:10.1002/fld.762

[25] Hoffren, J., Talonpoika, T., Larjola, J., and Siikonen, T., "Numerical Simulation of Real-Gas Flow in a Supersonic Turbine Nozzle Ring," *Journal of Engineering for Gas Turbines and Power*, Vol. 124, No. 2, April 2002, pp. 395–403. doi:10.1115/1.1423320

[26] Van der Stelt, T. P., Woudstra, N., Colonna, P., "Cycle-Tempo: A Program for Thermodynamic Modeling and Optimization of Energy Conversion Systems," Ver. 5.0, Delft University of Technology, Delft, The Netherlands, 1985–2004.

[27] Van der Stelt, T. P., and Colonna, P., "Fluidprop: A Program for the Estimation of Thermophysical Properties of Fluids," Energy Technology Section, Ver. 2.2, Delft University of Technology, Delft, The Netherlands, 2005, www.fluidprop.com.

[28] Rowley, R., Wilding, W., Oscarson, J., Yang, Y., Zundel, N., Daubert, T., and Danner, R., *DIPPR Data Compilation of Pure Chemical Properties*, Taylor and Francis, New York, 2004.

[29] Span, R., and Wagner, W., "Equations of State for Technical Applications. 1. Simultaneously Optimized Functional Forms for Nonpolar and Polar Fluids," *International Journal of Thermophysics*, Vol. 24, No. 1, Jan. 2003, pp. 1–39. doi:10.1023/A:1022390430888

[30] Colonna, P., Nannan, N. R., Guardone, A., and Lemmon, E. W., "Multiparameter Equations of State for Selected Siloxanes," *Fluid Phase Equilibria*, Vol. 244, No. 2, 2006, pp. 193–211. doi:10.1016/j.fluid.2006.04.015

[31] Nannan, N. R., Colonna, P., Tracy, C. M., Rowley, R. L., and Hurly, J. J., "Ideal-Gas Heat Capacities of Dimethylsiloxanes from Speed-of-Sound Measurements and Ab Initio Calculations," *Fluid Phase Equilibria*, Vol. 257, No. 1, 2007, pp. 102–113. doi:10.1016/j.fluid.2007.04.028

[32] Colonna, P., Nannan, N. R., and Guardone, A., "Multiparameter Equations of State for Siloxanes: $[(CH_3)_3\text{-Si-}O_{1/2}]_2$-$[O\text{-Si-}(CH_3)_2]_{i=1\ldots3}$, and $[O\text{-Si-}(CH_3)_2]_6$," *Fluid Phase Equilibria* (to be published).

[33] Lindley, D. D., and Hershey, H. C., "The Orthobaric Region of Octamethyltrisiloxane," *Fluid Phase Equilibria*, Vol. 55, Nos. 1–2, 1990, pp. 109–124.
doi:10.1016/0378-3812(90)85007-W

[34] Hurd, C. B., "Studies of Siloxanes. 1. The Specific Volume and Viscosity in Relation to Temperature and Costitution," *Journal of the American Chemical Society*, Vol. 68, No. 3, 1946, pp. 364–370.
doi:10.1021/ja01207a005

[35] Flaningam, O. L., "Vapor Pressures of Poly(Dimethylsiloxane) Oligomers," *Journal of Chemical and Engineering Data*, Vol. 31, No. 3, 1986, pp. 266–272.
doi:10.1021/je00045a002

[36] Ditsent, V. E., Skorokhodov, I. I., Terentéva, N. A., and Zolotareva, M. N., "Saturated Vapor Pressures of Polydiorganosiloxanes, II. Polydimethylcyclosiloxanes," *Russian Journal of Physical Chemistry A*, Vol. 45, No. 1, 1971, p. 1587.

[37] Marcos, D., Lindley, D., Wilson, K., Kay, W., and Hershey, H., "A (P, v, T) Study of Tetramethylsilane, Hexamethyldisiloxane, Octamethyltrisiloxane,and Toluene from 423 K to 573 K in the Vapor Phase," *Journal of Chemical Thermodynamics*, Vol. 15, No. 11, 1983, pp. 1003–1014.
doi:10.1016/0021-9614(83)90024-1

[38] McLure, I. A., Pretty, A. J., and Sadler, P. A., "Specific Volumes, Thermal Pressure Coefficients, and Derived Quantities of Five Dimethylsiloxane Oligomers from 25 to 140°C," *Journal of Chemical and Engineering Data*, Vol. 22, No. 4, 1977, pp. 372–376.
doi:10.1021/je60075a004

[39] Angelino, G., and Colonna, P., "Multicomponent Working Fluids for Organic Rankine Cycles (ORCs)," *Energy*, Vol. 23, No. 6, 1998, pp. 449–463.
doi:10.1016/S0360-5442(98)00009-7

[40] Nannan, N. R., Colonna, P., Tracy, C. M., Rowley, R. L., and Hurly, J. J., "Ideal-Gas Heat Capacities of Dimethylsiloxanes from Speed-of-Sound Measurements and Ab Initio Calculations," *Fluid Phase Equilibria* (to be published).

[41] Colonna, P., Rebay, S., Harinck, J., and Guardone, A., "Real-Gas Effects in ORC Turbine Flow Simulations: Influence of Thermodynamic Models on Flow Fields and Performance Parameters," *Proceedings of the ECCOMAS CFD 2006 Conference*, Egmond aan Zee, The Netherlands, 2006.

[42] Colonna, P., and Silva, P., "Dense Gas Thermodynamic Properties of Single and Multi-Component Fluids for Fluid Dynamics Simulations," *Journal of Fluids Engineering*, Vol. 125, No. 3, 2003, pp. 414–427.
doi:10.1115/1.1567306

[43] Selmin, V., "The Node-Centered Finite Volume Approach: Bridge Between Finite Differences and Finite Elements," *Computer Methods in Applied Mechanics and Engineering*, Vol. 102, No. 1, 1993, pp. 107–138.
doi:10.1016/0045-7825(93)90143-L

[44] Roe, P. L., "Approximate Riemann Solvers, Parameter Vectors, and Difference Schemes," *Journal of Computational Physics*, Vol. 43, No. 2, 1981, pp. 357–372.
doi:10.1016/0021-9991(81)90128-5

[45] Vinokur, M., and Montagné, J. L., "Generalized Flux-Vector Splitting and Roe Average for an Equilibrium Real Gas," *Journal of Computational Physics*, Vol. 89, No. 2, 1990, pp. 276–300.
doi:10.1016/0021-9991(90)90145-Q

[46] Colonna, P., Guardone, A., Harinck, J., and Rebay, S., "Numerical Investigation of Dense Gas Effects in Turbine Cascades," *Proceedings of the 15th U.S. National Congress on Theoretical and Applied Mechanics*, U.S. National Committee on Theoretical and Applied Mechanics, Washington, D.C., 2006.

[47] Arts, T., Lambert de Rouvroit, M., and Rutherford, A. W., "Aero-Thermal Investigation of a Highly Loaded Transonic Linear Turbine Guide Vane Cascade," Von Karman Institute for Fluid Dynamics, TN 174, Sept. 1990.

[48] E. W. Lemmon, R. T., Jacobsen, S. P., and Friend, D., "Thermodynamic Properties of Air and Mixtures of Nitrogen, Argon, and Oxygen from 60 to 2000 K at Pressures to 2000 MPa," *Journal of Physical and Chemical Reference Data*, Vol. 29, No. 3, 2000, pp. 331–385.
doi:10.1063/1.1285884

[49] Guardone, A., and Rebay, S., "Unstructured Periodic Grid Generation," *Proceedings of the ECCOMAS CFD 2006 Conference*, Egmond aan Zee, The Netherlands, 2006.

[50] Rebay, S., "Efficient Unstructured Mesh Generation by Means of Delaunay Triangulation and Bowyer–Watson Algorithm," *Journal of Computational Physics*, Vol. 106, No. 1, 1993, pp. 125–138.
doi:10.1006/jcph.1993.1097

[51] Giles, M., "Non-Reflecting Boundary Conditions for Euler Equation Calculations," *AIAA Journal*, Vol. 28, No. 12, 1990, pp. 2050–2058.

[52] Colonna, P., and Guardone, A., "Molecular Interpretation of Nonclassical Gas Dynamics of Dense Vapors Under the Van der Waals Model," *Physics of Fluids*, Vol. 18, No. 5, May 2006, pp. 1–14.

[53] Schnerr, G., and Leidner, P., "Diabatic Supersonic Flows of Dense Gases," *Physics of Fluids A*, Vol. 3, No. 10, 1991, pp. 2445–2458.
doi:10.1063/1.858183

C. Tan
Associate Editor